The impact of spin–orbit coupling on fine-structure and spin polarisation in photoexcited porphyrin triplet states

Gabriel Moise [a],[*],[1], Ashley J. Redman [a],[1], Sabine Richert [a],[b], William K. Myers [a], Ibrahim Bulut [c], Pernille S. Bolls [c], Michel Rickhaus [c], Jibin Sun [c], Harry L. Anderson [c], Christiane R. Timmel [a],[*]

[a] Centre for Advanced Electron Spin Resonance (CAESR), Inorganic Chemistry Laboratory, Department of Chemistry, University of Oxford, South Parks Road, Oxford, OX1 3QR, United Kingdom
[b] Institute of Physical Chemistry, University of Freiburg, Albertstraße 21, Freiburg, 79104, Germany
[c] Chemistry Research Laboratory, Department of Chemistry, University of Oxford, 12 Mansfield Road, Oxford, OX1 3TA, United Kingdom

ABSTRACT

The photoexcited triplet states of porphyrins show great promise for applications in the fields of opto-electronics, photonics, molecular wires, and spintronics. The magnetic properties of porphyrin triplet states are most conveniently studied by time-resolved continuous wave and pulse electron spin resonance (ESR). This family of techniques is singularly able to probe small yet essential details of triplet states: zero-field splittings, **g**-anisotropy, spin polarisation, and hyperfine interactions. These characteristics are linked to spin–orbit coupling (SOC) which is known to have a strong influence on photophysical properties such as intersystem crossing rates. The present study explores SOC effects induced by the presence of Pd^{2+} in various porphyrin architectures. In particular, the impact of this relativistic interaction on triplet state fine-structure and spin polarisation is investigated. These properties are probed using time-resolved ESR complemented by electron-nuclear double resonance. The findings of this study could influence the future design of molecular spintronic devices. The Pd^{2+} ion may be incorporated into porphyrin molecular wires as a way of controlling spin polarisation.

1. Introduction

Spintronic devices, as opposed to conventional electronic devices, exploit the spin degree of freedom of electrons as well as the charge for carrying out their function [1–7]. Such devices promise substantial improvements to many of the limitations encountered in classical electronics such as volatility, processing speeds, power consumption, and integration densities. This new paradigm of spin-based electronics envisages a range of multi-functional devices such as spin-FETs (field-effect transistors), spin-LEDs (light-emitting diodes), optical switches, and spin qubits. The synthetic tunability and versatility of organic π-conjugated molecules, of which porphyrins are preeminent examples, make them particularly attractive for incorporation into spintronic devices [4,6,7]. This desirable union between innovative spintronics and highly tunable molecules requires research into principles by which spin density can be generated in molecules, the ways in which spin delocalisation and spin polarisation can be modulated, and methods of coherent manipulation of the spin states. This work addresses precisely these issues. The porphyrins investigated here, shown in Fig. 1, provide

switchable access to spin density by means of photoexcitation. Furthermore, the presence or absence of metal ions within the porphyrin core modulates both electron spin delocalisation and spin polarisation. And finally, the methodology of ESR inextricably involves coherent manipulation of the spin degree of freedom.

Not far from the remit of spintronics, the development of more efficient and cost-effective organic light-emitting diodes [8,9] and organic photovoltaic cells [4,10] also demands progress in our understanding of the photo-induced dynamics of triplet state formation. Since one of the key interactions which leads to the formation of triplet states by intersystem crossing (ISC) is spin–orbit coupling (SOC), fundamental photophysics research into SOC mediated processes and properties has seen a substantial revival in recent years [11]. The present study of the photo-excited triplet states of porphyrins, particularly those containing Pd^{2+} (Fig. 1), further highlights the complexity of the SOC interaction and, in particular, its influence on fine-structure parameters and electron spin polarisation.

Oligoporphyrin architectures similar to the ones investigated here are examples of molecular wires which may be used in nano-scale
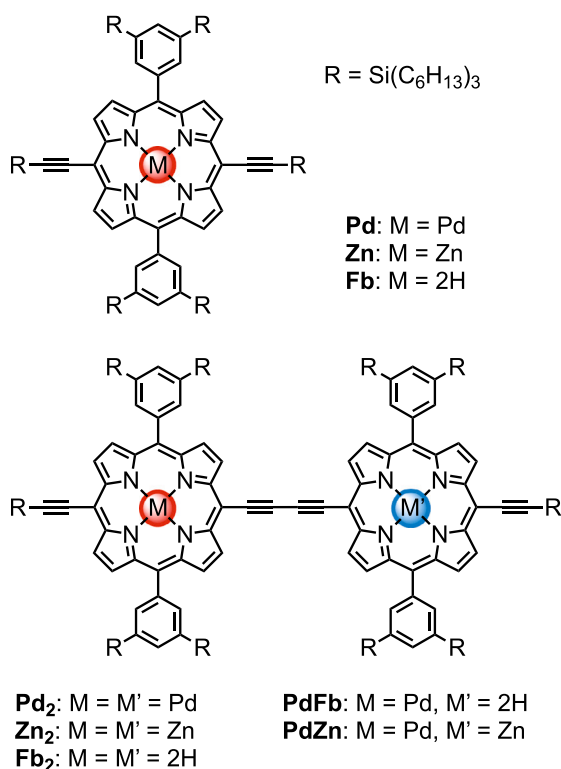

Fig. 1. Skeletal structures of the investigated porphyrin monomers and dimers. These molecules will be referred to using the following abbreviations: **Pd**, **Zn**, and **Fb** for the palladium(II), zinc(II), and free-base monomers, respectively; homodimers will be denoted by **Pd₂**, **Zn₂**, and **Fb₂**; the heterodimers are then naturally represented by **PdFb** and **PdZn**. Longer palladium(II) oligomers (up to the heptamer) are discussed in sections 2 and 3 of the SI.

electronic and spintronic devices [12–16]. Electron spin resonance (ESR) has long been at the forefront of research dedicated to the study of such porphyrin based molecular wires [17–31], and countless biologically relevant π-conjugated triplet states [32–37]. Although ESR plays an important role in the characterisation of paramagnetic porphyrin systems, only a handful of papers mention briefly the fine-structure and spin polarisation of palladium porphyrin triplet states [38–40]. The magnetic properties of these systems have yet to be described in any satisfying detail. Addressing this gap in the field of porphyrin molecular wires is important because the presence of Pd^{2+} is known to increase the triplet quantum yield and it will also have a significant impact on *any* interaction/property dependent on the relativistic SOC Hamiltonian [41–45]. As a result, particular emphasis will be placed in this work on the effect of Pd^{2+} mediated SOC effects on the magnetic properties of porphyrins (zero-field splittings, *g*-factors, and electron spin polarisation).

2. Theory and methods

This work employs transient ESR (trESR), pulse electron-nuclear double resonance (ENDOR), and magneto-photo-selection (MPS) experiments for studying the photoexcited triplet states of porphyrin systems. Because some of the molecules of interest here contain the heavy Pd^{2+} ion, it is necessary to introduce a framework which unites the SOC interaction with the existing porphyrin ESR methodologies [22,23,26, 29] which have hitherto only had minimal reliance on an understanding of relativistic effects. Such a union will be instrumental for data interpretation.

The ESR spectra of the photoexcited triplet states in this work are modelled well by the following phenomenological effective spin Hamiltonian:

$$\hat{H} = \frac{\mu_B}{\hbar} \mathbf{B} \cdot \mathbf{g} \cdot \hat{\mathbf{S}} + \hat{\mathbf{S}} \cdot \mathbf{D} \cdot \hat{\mathbf{S}} \tag{1}$$

where $\hat{\mathbf{S}}$ is the spin vector operator for triplet states ($S = 1$), $\mathbf{B}$ is the externally applied static magnetic field vector, and $\mathbf{g}$ and $\mathbf{D}$ are the Zeeman and zero-field splitting (ZFS) interaction tensors, respectively. In atomic structure theory, the relativistic corrections to the energy caused by the spin–orbit coupling and the spin–spin coupling (for example) are referred to as fine-structure interactions because they lead to small splittings within spectral lines. By analogy, since the $\mathbf{g}$- and $\mathbf{D}$-tensors also originate in the spin–orbit and spin–spin interactions, these two terms in the spin Hamiltonian may also be categorised as fine-structure interactions. The next section outlines the different contributions to $\mathbf{g}$ and $\mathbf{D}$ with the aim of uniting previous porphyrin triplet state ESR theory with the SOC interaction, thus facilitating subsequent discussions of the data.

2.1. The origins of **g** and **D**

Two particular interactions, spin–spin coupling (SSC) and spin–orbit coupling (SOC), are often sufficient for understanding the ESR spectra of organic triplet states. To first-order in perturbation theory, SSC contributes only to the **D**-tensor. To second-order in perturbation theory, the SOC interaction leads to **g**-tensor anisotropy and also to a second contribution to the **D**-tensor. The discussion that follows is a summary drawn from the most relevant aspects in the literature regarding the origin of ESR parameters [46–51]. Less general expressions for **g** and **D** may be found in textbooks [52–54].

The SSC contribution to the **D**-tensor is given by the following formula:

$$\mathbf{D}_{SSC} = \frac{\mu_0}{8\pi} g_e^2 \left(\frac{\mu_B}{\hbar} \right)^2 \left\langle \sum_{i,j>i} \frac{1 - 3\hat{\epsilon}_{ij} \otimes \hat{\epsilon}_{ij}}{\hat{r}_{ij}^3} \right\rangle \tag{2}$$

where the angular brackets indicate integration over the spatial part of the triplet wavefunction, g_e is the free-electron *g*-value, $\otimes$ indicates the outer product of two vectors, $\hat{\mathbf{r}}_{ij}$ is the inter-electron position vector, $\hat{\epsilon}_{ij}$ is the corresponding unit vector, and the double sum extends over all unique pairs of electrons (indexed by i and j).

As mentioned, the SOC interaction contributes to both **g** and **D** as a second-order perturbation. Assuming that the triplet state of interest is perturbed by only one other triplet state with relative energy Δ, the **g**-tensor is:

$$\mathbf{g} = g_e \mathbf{1} - \frac{\sqrt{2}}{\hbar} \frac{\mathcal{L} \otimes \zeta}{\Delta} \tag{3}$$

In this equation, $\mathcal{L}$ is the matrix element of the total orbital angular momentum between the spatial parts of the two triplet wavefunctions, *i.e.* $\mathcal{L} = \langle a | \sum_i \hat{\mathbf{l}}_i | b \rangle$ where a is the triplet state of interest, b is the closest excited triplet state, and the sum extends over the individual angular momenta of each electron (indexed by i). Both a and b are the spatial parts of triplet state wavefunctions as there are no contributions to **g** from states of different multiplicity. Additionally, for non-degenerate (*i.e.* real) spatial wavefunctions, there is no first-order contribution to **g** because each of the $\hat{\mathbf{l}}_i$ operators is imaginary, *i.e.* there is no contribution to **g** from the triplet state of interest (labelled by a). ζ is a vector with components given by *reduced* matrix elements of the spin–orbit coupling Hamiltonian between the b and a states, *i.e.* the components of this vector are given by:

$$\zeta_q = \langle b || \hat{H}_{SOC}^q || a \rangle = \langle b || \sum_i \hat{\lambda}_i \hat{l}_i^q \hat{s}_i || a \rangle \tag{4}$$

where $q \in \{x, y, z\}$ and $\hat{\lambda}_i$ is a scalar operator related to the gradient of the electron-nuclear potential energy [11,55]. Both $\mathcal{L}$ and ζ are Cartesian vectors with purely imaginary components. Although irrelevant for our purposes, the factor of $\sqrt{2}$ in Eq. (3) is a consequence of the fact that the components of ζ are *reduced*, rather than full, matrix

elements; the emergence of this S-dependent factor can be understood by following the derivation of Neese and Solomon [56].

Assuming again that only one excited triplet state perturbs the triplet state of interest, the second-order SOC contribution to the **D**-tensor is given by:

$$\mathbf{D}_{\text{SOC}} = \frac{1}{6\hbar} \Delta^{-1} \left(\zeta^* \cdot \zeta - 3\zeta^* \otimes \zeta \right) \tag{5}$$

where $*$ denotes complex conjugation and the factor of 6 is again a consequence of ζ being a reduced matrix element.

Generally, the total **D**-tensor, $\mathbf{D} = \mathbf{D}_{\text{SSC}} + \mathbf{D}_{\text{SOC}}$, has three eigenvalues D_x, D_y, and D_z corresponding to three orthogonal eigenvectors which have a fixed orientation relative to the molecule. This set of eigenvectors defines the eigenframe of **D**, and the eigenvalues are labelled in accordance with the convention: $|D_y| \leq |D_x| \leq |D_z|$. Assuming that the eigenframes of $\mathbf{D}_{\text{SSC}}$ and $\mathbf{D}_{\text{SOC}}$ have collinear axes, each of these eigenvalues may be written as a sum of SSC and SOC contributions (albeit, the 'xyz' labelling of each contribution may be different). This assumption is consistent with the experimental results reported here. However, since the total **D**-tensor is chosen to be traceless, we may restrict our attention to only two independent parameters:

$$D = \frac{3}{2} D_z \tag{6}$$

$$\lambda = \left| \frac{E}{D} \right| = \frac{1}{3} \left| \frac{D_x - D_y}{D_z} \right| \tag{7}$$

These definitions of D and λ are the same regardless of the origin of the ZFS interaction. Note that the D-value may still be decomposed into SSC and SOC contributions, $D = D_{\text{SSC}} + D_{\text{SOC}}$, whereas λ cannot (however, λ_{SSC} and λ_{SOC} may still be defined). Regardless of origin, the D-value is the axial ZFS parameter, and $\lambda \in [0, 1/3]$ is the orthorhombicity parameter.

The link between the fine-structure parameters introduced in Eqs. (2)–(7) and molecular symmetry will be very important for this work. The points made in this paragraph relate only to the SSC contribution to the **D**-tensor. These issues have also been described previously [22,23,26]. When $\lambda_{\text{SSC}} = 0$, the spin density is axially symmetric, and when $\lambda_{\text{SSC}} = 1/3$, the spin density is (maximally) orthorhombic. By reference to the symmetries of spheroids, the triplet spin density may be classified as being prolate or oblate. The former corresponds to a negative D_{SSC}-value, whereas the latter corresponds to a positive D_{SSC}-value. Furthermore, in the case of oblate spin densities, the eigenvector of $\mathbf{D}_{\text{SSC}}$ associated with the $D_{z,\text{SSC}}$ eigenvalue is parallel to the minor axis of the spheroid. For prolate spin densities, the same eigenvector is parallel to the major axis of the spheroid.

By contrast, the symmetry properties of the **g** and $\mathbf{D}_{\text{SOC}}$ tensors cannot be connected to the spheroidal symmetry of the spin density. These two tensors are related to both the symmetry species of the triplet wavefunction of interest and the symmetry species of the excited triplet state(s). This issue will be explored below in the context of the ESR data obtained on the palladium porphyrin systems.

2.2. Electron spin polarisation

The triplet states investigated here are formed by photoexcitation in the presence of a magnetic field followed by an ISC event mediated by the SOC interaction. Hence, the spin sub-level populations are not at equilibrium and the ensemble is said to be spin polarised. In the interest of simplicity, the following assumptions are made: (1) the ISC event happens within the limits of the Fermi golden rule, *i.e.* coherences are neglected, (2) only one crossover event is relevant, *i.e.* from the first excited singlet state to the triplet state of interest, (3) relaxation and anisotropic kinetic effects are ignored, (4) the impact of the magnetic field strength and orientation is determined exactly by the overlap of the zero-field eigenstates with the true eigenstates of $\hat{H}$

from Eq. (1). The final assumption means that the populations, P_ψ, of the true eigenstates, $|\psi\rangle$, are computed according to [26]:

$$P_\psi = P_x |\langle X|\psi\rangle|^2 + P_y |\langle Y|\psi\rangle|^2 + P_z |\langle Z|\psi\rangle|^2 \tag{8}$$

where $|X\rangle$, $|Y\rangle$, and $|Z\rangle$ are the eigenstates of the ZFS Hamiltonian, $\hat{\mathbf{S}} \cdot \mathbf{D} \cdot \hat{\mathbf{S}}$, with eigenvalues $-D_x$, $-D_y$, and $-D_z$, respectively, and P_x, P_y, P_z are the zero-field populations.

Within the Fermi golden rule limit, the population P_q with $q \in \{x, y, z\}$ (at zero field) is related to the reduced matrix element of $\hat{H}^q_{\text{SOC}}$ according to:

$$P_q \propto \left| \langle S || \hat{H}^q_{\text{SOC}} || T \rangle \right|^2 \equiv |\xi_q|^2 \Longleftrightarrow \mathbf{P} = \xi^* \odot \xi \tag{9}$$

where $|S\rangle$ and $|T\rangle$ are the *spatial* parts of the singlet and triplet wavefunctions, including the vibrational part. The imaginary number ξ_q is a component of a Cartesian vector, ξ, encapsulating the SOC reduced matrix element along with any proportionality factors. Therefore, the population vector **P** is the Hadamard product, $\odot$, of ξ^* and ξ. Since $\hat{H}^q_{\text{SOC}}$ depends on the gradient of the electron-nuclear potential energy, it will depend on the positions of the nuclei, and by extension, on the vibrational mode coordinates. For simplicity, suppose there exists a SOC active mode. To first-order in perturbation theory, ξ may be expanded around the matrix element of the mode coordinate, ν:

$$\xi \approx \xi^0 + \partial \xi^0 \nu \tag{10}$$

where ξ^0 is the (vectorised) equilibrium SOC matrix element, and $\partial \xi^0$ is the derivative of ξ with respect to the mode coordinate evaluated at the expansion point. By substituting Eq. (10) into (9):

$$\mathbf{P} = \xi^{0*} \odot \xi^0 + 2\partial \xi^{0*} \odot \xi^0 \nu + \partial \xi^{0*} \odot \partial \xi^0 \nu^2. \tag{11}$$

Therefore, three different mechanisms leading to spin polarisation may be distinguished [11,55]: (1) the direct/Franck–Condon mechanism driven by the first term in the equation above, (2) the mixed Franck–Condon/Herzberg–Teller mechanism driven by the middle term, (3) the pure Herzberg–Teller/vibronic mechanism driven by the final term. The symmetry constraint on the direct mechanism is dictated by the symmetry species of the singlet and triplet wavefunctions as well as by the symmetry of $\hat{H}^q_{\text{SOC}}$, which is equivalent to the symmetry species of the rotation matrices around the q-axis. This leads to the usual El Sayed rules [57]. The pure vibronic mechanism relaxes the El Sayed rules in the presence of a vibrational mode with a sufficiently large mode derivative, $\partial \xi^0$, and an appropriate symmetry species. The mixed mechanism is subject to both the El Sayed and the vibronic coupling selection rules. In organic chromophores without heavy elements (*e.g.* the $\mathbf{Fb_n}$ systems), the direct and mixed mechanisms are intuitively expected to be small. Hence, the vibronic mechanism is the prime suspect for the emergence of spin polarisation in such systems. This is consistent, for example, with the experimental observations of van Dorp et al. [58], Tait et al. [22,23] and with the present work.

2.3. Experimental methods

Synthesis and characterisation. The **Pd** system was prepared from the **Fb** system using the same procedure as shown in the SI for $\mathbf{Pd_2}$ and reported previously by Therien and coworkers [44,45]. All relevant synthetic procedures for the dimer systems introduced in Fig. 1 are given in section 1 of the SI.

Transient ESR (trESR). The samples were prepared to an oligomer (monomer/dimer) concentration of ca. 200 μM using 2-methyltetrahydrofuran. The X-band trESR spectra were recorded at 20 K using a Bruker ELEXSYS E680 spectrometer with an EN 4118X-MD4-W1 resonator. The laser light was directed through the optical window of the cryostat. Laser excitation was performed with depolarised light at 532 nm using an Opotek Opolette HE 355 LD optical parametric oscillator pumped by the third harmonic of a Nd:YAG laser. The excitation energy was ca. 2 mJ at a repetition rate of 20 Hz. All data

Table 1
Best fit values of the ZFS parameters (D and λ), relative sub-level populations (the population/polarisation vector, **P**), and g-values obtained from simulations of the data shown in Fig. 2. All subscripts (x, y, z) refer to the eigenframe of the **D**-tensor (described in more detail later with reference to Figs. 4, 6 and 7). For the new systems, the signs of the D-values were determined via ENDOR and MPS experiments, as discussed in the main text. As part of the supporting files, we provide a compilation of the following: *.mat* files containing all data from Fig. 2, and *.m* files containing the simulation scripts with all simulation parameters including *HStrain* and *DStrain*. For the purposes of the discussion, the following approximate uncertainties should be assumed: ± 10 MHz for D, ± 0.05 for λ, ± 0.05 for the elements of **P**, and ± 0.001 for the elements of **g**.

System	D / MHz	$\lambda = |E/D|$	$\mathbf{P} = (P_x, P_y, P_z)$	$\mathbf{g} = (g_x, g_y, g_z)$
Pd	−2271	0.00	(1.00, 0.00, 0.00)	(1.966, 2.011, 2.006)
Zn	+906	0.18	(0.12, 0.00, 0.88)	(2.006, 2.007, 2.004)
Fb	+1024	0.14	(0.50, 0.50, 0.00)	(2.009, 2.009, 2.008)
Pd$_2$	−2367	0.05	(0.92, 0.08, 0.00)	(1.983, 2.006, 2.005)
Zn$_2$	−1125	0.22	(0.95, 0.00, 0.05)	(2.006, 2.007, 2.007)
Fb$_2$	−1029	0.28	(0.00, 0.20, 0.80)	(2.007, 2.001, 2.009)
PdZn	−1109	0.27	(0.95, 0.05, 0.00)	(2.005, 2.007, 2.009)
PdFb	+1020	0.26	(0.00, 0.14, 0.86)	(2.007, 2.007, 2.006)

analysis and simulations were performed using the EasySpin package in MATLAB [59]. All trESR data displayed throughout this work have been corrected to a common microwave frequency of 9.75 GHz. This correction of the field axis is valid because the systems are in the high-field limit. The displayed spectra are obtained from the time domain data by averaging over a time window of 1.2 μs (the normalised spectra do not change significantly with the length and position of the time averaging window). Further experimental results are shown in the SI accompanied by the relevant acquisition details.

Magneto-photo-selection (MPS). The MPS experiments were performed to determine the orientation of the **D**-tensor relative to the optical transition dipole moments of the molecule. The data were collected analogously to the trESR data, with the exception of the wavelength and polarisation of the laser light (these are stated in the relevant figure captions). Care was taken to ensure identical pulse energies for each polarisation. The data were simulated according to the methodology described by Tait et al. [60].

Electron-nuclear double resonance (ENDOR). The proton hyperfine couplings in these systems were investigated at 20 K using the Mims ENDOR pulse sequence employing 16 ns microwave pulses, a 15 μs radiofrequency pulse, and by tau-averaging stimulated echo delays of 120, 180, and 240 ns, as per previously published results on similar systems [22,23,26,29]. All ENDOR spectra were obtained by laser excitation at 532 nm.

3. Results and discussion

The experimental trESR spectra of the porphyrin systems are shown in Fig. 2 together with the results of numerical simulations. The most relevant simulation parameters are collated in Table 1. The **Zn**, **Zn$_2$**, **Fb**, and **Fb$_2$** systems have been extensively characterised by ESR in previous publications, such as in the work of Tait et al. [22,23] It is now necessary to give a brief account of the known properties of these four species before proceeding to elucidate the ZFS, **g**-tensors and spin polarisation properties of the new systems.

3.1. The **Zn** and **Fb** systems

The **Zn** and **Fb** monomer systems have a positive D-value corresponding to a situation where the D_z principal axis is perpendicular to the porphyrin macrocycle. Although the orthorhombicity parameters, λ, of these species is close to 1/6 (the midpoint between axial and orthorhombic), the positive D-value is in keeping with the expected quasi-oblate symmetry of the triplet spin density. The D-value in both **Zn** and **Fb** primarily stems from the SSC contribution shown in Eq. (2). The similarity of the D- and λ-values indicates that the average distance between the electron spins is similar in the two monomers suggesting similar spin densities. The slight reduction of D in the **Zn** system could be attributable to a small and negative contribution from SOC [56].

The **Zn** spectrum is essentially an 'upside down' version of the **Fb** spectrum as reflected by the spin polarisation parameters in Table 1. In **Fb**, the absence of heavy elements means that the ISC mechanism is driven purely vibronically as discussed in the previous section. Calculations by Perun et al. [61] suggest that free-base porphyrins indeed have spin–orbit active vibrational modes which drive ISC via the Herzberg–Teller mechanism. These spin–orbit active modes involve *gerade* displacements of the peripheral carbon atoms of the unprotonated pyrrole rings in **Fb** [61]. Within the D_{2h} point group, the symmetries of these modes are B_{2g} and B_{3g} [61]. As will be discussed later, these vibrations are of the right symmetry to promote the observed in-plane spin polarisation of **Fb** (because $D > 0$, the in-plane axes correspond to P_x and P_y). By contrast, the **Zn** spin polarisation is primarily in the out-of-plane (P_z) direction [62,63]. This effect has been shown to originate in the direct SOC mechanism [58,64]. The small non-zero value of P_x in **Zn** could be a result of the vibronic mechanism [22]. The fact that the SOC interaction is strong enough to affect the spin polarisation of **Zn** but not the **D** or **g**-tensors is unsurprising; as discussed, the former effect is first-order in perturbation theory whereas the latter tensors are second-order in the SOC interaction.

3.2. The **Pd** system

The trESR spectrum of **Pd** is strikingly different to the spectra of the other monomer systems: it is wider by almost a factor of two due to a larger $|D|$-value of 2271 MHz, and it is asymmetric due to a larger **g**-anisotropy. The asymmetry is more pronounced in the W-band data shown in Figure S14 of the SI. If the D-value is assumed to be negative, the sub-level population vector is (1.00, 0.00, 0.00) as shown in Table 1. On the other hand, if the D-value is assumed to be positive, the same simulated spectrum is obtained with a population vector given by (0.00, 0.50, 0.50). From the symmetry arguments presented later in this paper, this latter spin polarisation pattern implied by a positive D-value would be highly unusual. In order to confirm that D is in fact negative in **Pd**, MPS and ENDOR experiments were carried out as will be shown now.

MPS is an effect observed in trESR experiments which may be employed for the determination of the orientation of the **D**-tensor of photoexcited triplet states relative to an optical transition dipole moment, τ, of the molecule [22,29,65–67]. The measurements are done in frozen glassy solutions such that the molecular orientations relative to the static external magnetic field are fixed. If the electric field of the incoming laser light is denoted by **E**, then the probability that the molecule undergoes a transition is proportional to the square of the scalar product $\mathbf{E} \cdot \tau$. For example, if τ is parallel to the polarisation of the incoming laser, the molecule has the largest probability of being photoexcited and eventually forming a triplet state. In MPS, two trESR spectra are typically recorded: one with the polarisation of the laser
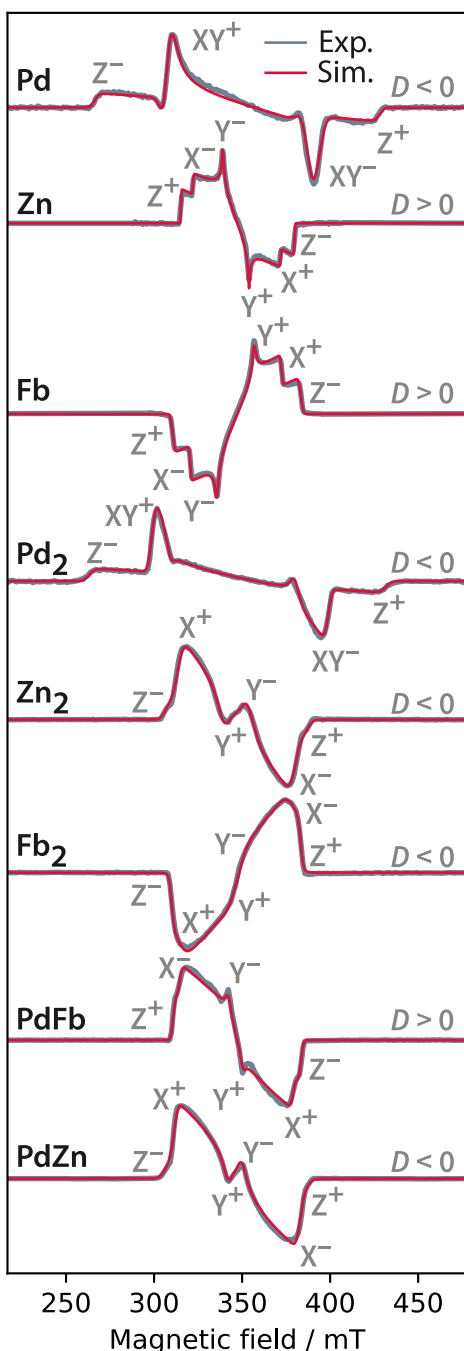
Fig. 2. X-band trESR data and numerical spectral simulations for the species depicted in Fig. 1. The associated simulation parameters are shown in Table 1. The turning points of each of the ESR spectra are labelled as $Q^{\pm}$ where $Q \in \{X, Y, Z\}$ refers to the orientations of the **D**-tensor which are resonant at the field position of the relevant turning point. For example, X means that the signal originates in molecules which have D_x aligned parallel to the static external magnetic field. The $\pm$ superscript denotes the pair of triplet sub-levels involved in the transition: the + refers to the $M_S = 0 \rightarrow +1$ transition and the - refers to the $M_S = -1 \rightarrow 0$ transition. All spectra have been normalised to the absolute maximum and were stacked for display purposes. Positive/negative peaks represent microwave absorption/emission. The assignment of the signs of D is discussed in the text.

parallel to the external magnetic field, and another with perpendicular polarisation. In the first case, $\mathbf{E} \parallel \mathbf{B}$, the laser preferentially selects molecules which have τ closely aligned to **B**. In the second case, $\mathbf{E} \perp \mathbf{B}$, the laser preferentially selects molecules which have τ perpendicular to **B**. Since the **D**-tensor orientation is fixed relative to τ, the two trESR

spectra will show enhanced intensity in features corresponding to the axes of **D** which have been preferentially selected. Strictly speaking, it is not the axes of **D** which are selected but rather molecular orientations which correspond to particular anisotropic distribution patterns of the orientation of **D** relative to **B**.

For the porphyrin systems investigated here, the link between the orientation of the **D**-tensor in the molecular frame and the sign of the D-value will be necessary in order to interpret the MPS results. When $D > 0$, the D_z axis is perpendicular to the porphyrin plane(s), and when $D < 0$, the D_z axis lies within the porphyrin plane(s). Furthermore, for the systems investigated here (including **Pd**), the optical transitions occurring in the Q-band region of the UV–Vis absorption spectra (above ca. 500 nm, see Figures S1–2) are known to correspond to transition dipole moments, τ, which lie close to the porphyrin plane [68,69]. This fact can also be gleaned from the group theoretical arguments discussed later (see Fig. 5). Note that for the purposes of interpreting the MPS results, it is not necessary to specify the x/y label of the transition dipole moment (the knowledge that τ is close to the porphyrin plane is enough for our purposes). The MPS data recorded for the **Pd** system are shown in Fig. 3 alongside the results of numerical simulations performed as mentioned in the 'Theory and methods' section. At either of the excitation wavelengths, the simulations predict that τ is within $\alpha = 35$–$36°$ of the D_z axis, and so, it is close to (although not exactly within) the porphyrin plane. The fact that α is not exactly zero from the simulations may also be caused by the many possible sources of error associated with MPS data interpretation as discussed in detail in previous work [29]. Fortunately, a qualitative inspection of the data in Fig. 3 already provides compelling enough evidence as to the orientation of **D** in the **Pd** system. At 550 nm, the spectrum with $\mathbf{E} \parallel \mathbf{B}$ shows a pronounced reduction in the signal corresponding to the XY transitions (by comparison with the $\mathbf{E} \perp \mathbf{B}$ data). Therefore, the D_x and D_y axes are effectively perpendicular to τ. The same effect is observed in the 588 nm data, but now with an additional important observation: at this wavelength, when $\mathbf{E} \parallel \mathbf{B}$, the Z transition is enhanced relative to the $\mathbf{E} \perp \mathbf{B}$ spectrum implying that D_z is closely aligned with τ, *i.e.* $D < 0$.

The second piece of evidence for D being negative in **Pd** comes from comparing its Mims ^{1}H-ENDOR spectra with the equivalent data for **Zn** as shown in Fig. 4. Before discussing the data, it is important to mention some of the key features observed in ENDOR spectra of triplet electronic states coupled to spin-1/2 nuclei. When the bandwidths of the microwave pulses are smaller than the frequency difference between the $M_S = -1 \rightarrow 0$ and $M_S = 0 \rightarrow +1$ transitions (which is true in our case), these electronic transitions may be excited selectively. Therefore, the ENDOR spectra will be asymmetric relative to the nuclear Larmor frequency. Additionally, all such spectra will contain a sharp peak at the Larmor frequency which comes from nuclei coupled to the $M_S = 0$ electronic state. Furthermore, the position of a particular peak relative to this Larmor peak depends on the sign of the hyperfine coupling and on whether the measurement is done on the $M_S = -1 \rightarrow 0$ or $M_S = 0 \rightarrow +1$ transition. In turn, the identity of the electronic transition at a particular field point is linked to the sign of D (as shown, for example, in Fig. 2). For example, positive hyperfine couplings appear on the left of the Larmor peak when the ENDOR measurement is conducted on the $M_S = 0 \rightarrow +1$ transition.

The **Zn** data (Fig. 4, left) have been discussed previously in the literature, as has the sign of D in this system [22,23,26]. For the purposes of this discussion, it suffices to focus our attention on two important characteristics: the peaks corresponding to the largest hyperfine coupling (assigned by Tait et al. [23] to the beta proton adjacent to the ethyne group), and the position of these peaks relative to the Larmor peak at $\nu_{rf} - \nu_H = 0$. The orientation of **D** (and sign of D) in **Pd** can be determined from ENDOR only if the orientation of the hyperfine tensors is known *a priori*. Therefore, in order to interpret the ENDOR data in Fig. 4, the following assumption is required: the spin density distribution of **Pd** is almost the same as for **Zn**. From an experimental
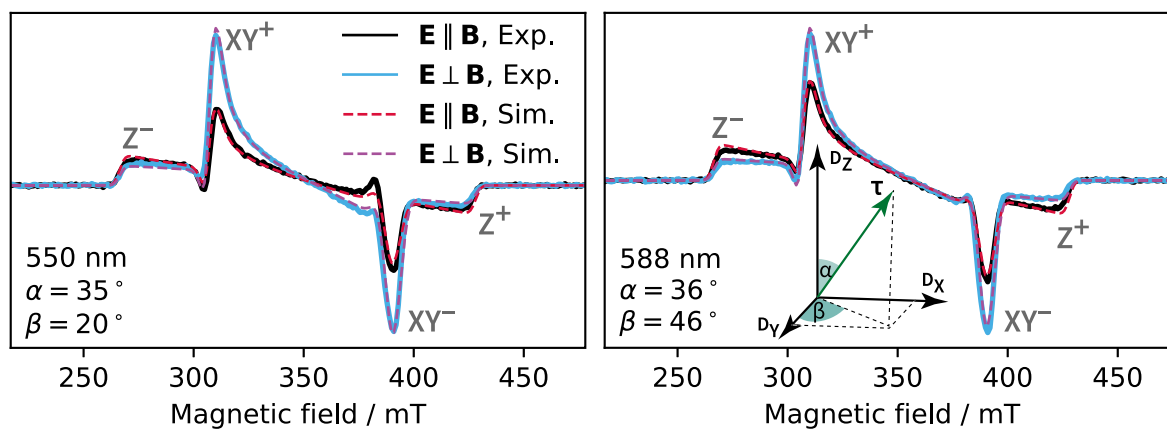
Fig. 3. Experimental and simulated X-band MPS data for the palladium monomer porphyrin, **Pd**. Two pairs of spectra were obtained by photoexcitation at 550 nm (left panel) and 588 nm (right panel). These wavelengths contribute to the Q-band region of the UV–Vis spectra shown in Figures S1–2 of the SI. The solid black lines correspond to light polarised parallel to the magnetic field of the ESR spectrometer, whereas the spectra in solid blue correspond to perpendicular polarisation. The simulations are shown by the dashed red and magenta lines. The α and β angles refer to the orientation of the transition dipole moment, τ, relative to the axes of the **D**-tensor as indicated by the inset in the right panel.
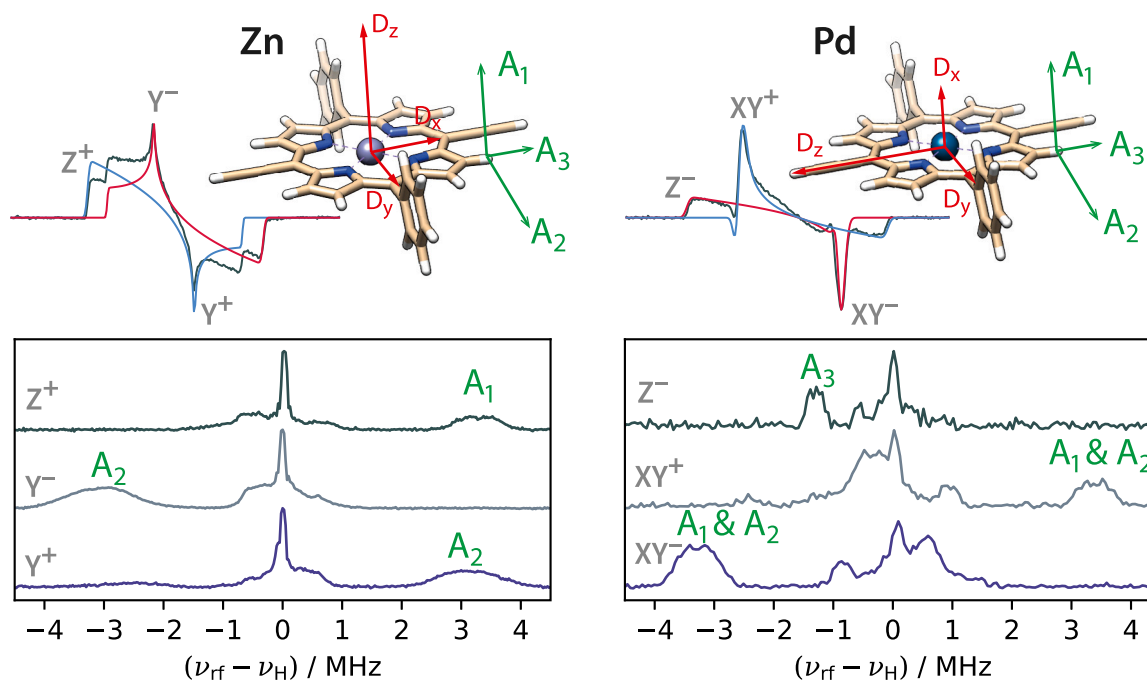

Fig. 4. Summary of Mims ^{1}H-ENDOR data for **Zn** and **Pd** acquired at the field positions indicated by $Q^\pm$ in the diagrams of the trESR spectra shown above the two main panels. The relative orientation of the **D**-tensor is shown as the red vectors overlaid on the molecular structure of each system (inferred from the ENDOR data shown here and the MPS results in Fig. 3). The green arrows represent the projections of the beta-proton hyperfine tensor axes onto the principal axes of the **D**-tensor (corresponding to the largest magnitude hyperfine couplings). Hence, these arrows are shown as parallel to the eigenframe of **D**. The 123 labelling scheme was chosen instead of the more usual xyz scheme because the interpretation of the ENDOR spectra is much clearer when a gauge-independent labelling scheme is adopted for the hyperfine projections. The blue and red lines superimposed on the trESR spectra correspond to simulations of the individual sub-spectra of the $M_S = 0 \to +1$ and $M_S = -1 \to 0$ sub-level transitions, respectively. As discussed in the main text, the main hyperfine tensor of the two systems is assumed to be approximately the same both in magnitude and orientation relative to the molecular frame. The **D**-tensor of the **Pd** system is reoriented relative to **Zn**, such that the D_z axis is within the porphyrin plane, as per the discussion in the main text.

point of view, this assumption is validated by the fact that almost all the peaks observed in the ENDOR spectra of **Pd** can be approximately mapped to peaks in the **Zn** ENDOR data (albeit, at different field positions and, by extension, **D**-tensor axes). From a theoretical point of view, Figure S19 of the SI shows the results of spin density calculations on **Zn** and **Fb** employing the complete active space self consistent field (CASSCF) method. The similarity of the CASSCF spin densities of **Zn** and **Pd**, depicted in the SI, provides further evidence that the largest hyperfine coupling tensor in both systems has approximately the same magnitude and orientation relative to the porphyrin backbone.

The left-most (low-field) peak in the trESR spectrum of **Zn** is known to represent the Z^+ transition because $D > 0$ in this system, *i.e.* it corresponds to the D_z axis of the ZFS tensor and to the $M_S = 0 \to +1$ transition. The ENDOR spectrum recorded at this field position therefore contains peaks originating in the projections of the hyperfine tensor(s) on the D_z axis. In particular, the largest such hyperfine coupling is the peak in the 3–4 MHz region marked with A_1 in the left panel of Fig. 4. For **Pd**, the exact same peak appears in the ENDOR data recorded on the low-field XY position in the trESR spectrum. Therefore, given the above discussion about the similarity of the spin densities of **Zn** and **Pd**, the low field XY transition of **Pd** must belong to the
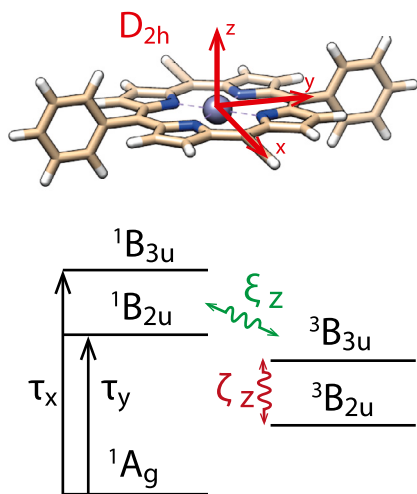
Fig. 5. (Top) Structure of a porphyrin monomer system and assignment of the molecular axes based on the assumption that the system is approximately D_{2h} symmetric. (Bottom) Proposed energy level diagram (not to scale) of a porphyrin monomer system showing the ground singlet state, ^1A_g, and two excited triplet and singlet states of B_{2u} and B_{3u} symmetry. The transition dipole moments of the optical excitation are represented as τ_x and τ_y; the subscript indicates the molecular axis along which the direct product of the dipole moment operator ($B_{1u} \rightarrow z$, $B_{2u} \rightarrow y$, $B_{3u} \rightarrow x$) is totally symmetric under the D_{2h} direct product table. The wavy arrows indicate non-zero elements of the spin–orbit coupling vectors ζ and ξ introduced in section 2. The spin–orbit operator, $\sum_i \lambda_i \hat{l}_i^q \hat{s}_i$, is assumed to transform as the R_q rotation matrix within the D_{2h} point group, i.e. $B_{1g} \rightarrow R_z$, $B_{2g} \rightarrow R_y$, $B_{3g} \rightarrow R_x$. As explained in the main text, the difference between the **Fb**, **Zn**, and **Pd** electronic states is mainly driven by the presence/absence of a significant LCAO d-orbital coefficient on the transition metal.

$M_S = 0 \rightarrow +1$ transition, i.e. it is the XY^+ transition and hence, $D < 0$ for **Pd**. Furthermore, the **Pd** spectrum recorded at the Z^- position shows a smaller main hyperfine coupling between 1–2 MHz (labelled by A_3). This coupling is also observed faintly in the **Zn** data recorded on the X^- transition reported by Tait et al. [22].

Another noteworthy difference between the **Zn** and **Pd** systems is that for the latter, the orthorhombicity parameter, λ, is very close to zero. This is the reason why the transitions in Fig. 4 are labelled by XY in **Pd** and only by Y in **Zn** (which has $\lambda = 0.18$). Furthermore, this fact also implies that the 3–4 MHz peak of **Pd** corresponds to the projections of the hyperfine tensor on both D_x and D_y axes, i.e. A_1 and A_2. Indeed, the same 3–4 MHz peak is observed very clearly in the $Y^\pm$ data shown here for **Zn** and the $Z^\pm$ data reported by Tait et al. [23].

The above arguments, strongly imply that $D < 0$ for **Pd**, and thus, the D_z axis is in the plane of the porphyrin. It seems now prudent to justify this fact from the perspective of the electronic structure of the molecule. This problem is most clearly resolved by group theoretical arguments which will shed more light on the origin of **D** in **Pd** and on the ISC mechanism in this species. The porphyrin monomers are considered to have an approximate D_{2h} symmetry (with Cartesian axes depicted in Fig. 5) and the frontier molecular orbitals are taken as a_u, b_{1u}, b_{2g}, and b_{3g}, by performing a descent in symmetry, $D_{4h} \rightarrow D_{2h}$, on the well-known Gouterman four-orbital model (which mostly assumes the D_{4h} point group) [69]. The electronic states resulting from this model are depicted in Fig. 5. The ground state of the molecules will be $|^1A_g\rangle$ corresponding to the $a_u^2 b_{1u}^2$ configuration. The excited states are $|^1B_{2u}\rangle/|^3B_{2u}\rangle$ from the $a_u^2 b_{1u}^1 b_{3g}^1$ configuration, and $|^1B_{3u}\rangle/|^3B_{3u}\rangle$ from the $a_u^2 b_{1u}^1 b_{2g}^1$ configuration. The energetic ordering of the states shown in Fig. 5 is consistent with the literature on Pd^{2+} porphyrins [68,69]. Despite the fact that the ordering of the electronic states will have no impact on the symmetry arguments below, we explore each of the $4! = 24$ possible orderings of the 4 excited states in the SI.

For **Zn** and **Pd**, the nature of the triplet SOMO, b_{2g}, and triplet LUMO, b_{3g}, is expected to be different compared to the **Fb** system. The

metal d_{xz} and d_{yz} orbitals have the right symmetry to mix with these orbitals. Therefore, the excited state wavefunctions (for both singlet and triplet states) will have a significant LCAO coefficient on these metal based orbitals. The greater radial extent of the palladium $4d$-orbitals leads to larger overlap with the porphyrin orbitals and significant LCAO coefficients on the palladium centre. For these reasons, the effects of SOC will manifest themselves in the **Pd** system most strongly not least because it also contains the heaviest metal. These aspects were also noted briefly in the work of Mulyana and Ishii [40].

The spin–orbit coupling Hamiltonian transforms approximately as one of the R_q rotation matrices, i.e. $B_{1g} \rightarrow R_z$, $B_{2g} \rightarrow R_y$, $B_{3g} \rightarrow R_x$. Therefore, by taking direct products in the D_{2h} point group, the ζ vector (Eq. (5)) is along the *molecular* z-axis:

$$\zeta = \begin{pmatrix} 0 \\ 0 \\ \zeta_z \end{pmatrix} \tag{12}$$

where $\zeta_z = \langle ^3B_{3u}||\hat{H}_{SOC}^z||^3B_{2u}\rangle$. We *emphasise* once more that the z subscript of ζ_z in Eq. (12) refers to the molecular frame defined by the D_{2h} point group (Fig. 5), not the eigenframe of **D**. By applying Eqs. (5) and (7), the SOC contribution to the D-value may be evaluated:

$$D_{SOC} = -\frac{|\zeta_z|^2}{3\hbar\Delta}. \tag{13}$$

It is therefore obvious that the SOC contribution leads to a reduction in the net D-value. For **Fb** and **Zn**, this contribution probably only has a small effect potentially evidenced by a slight reduction in D from the former to the latter (Table 1). However, the value of ζ_z is expected to be much larger for the **Pd** system, as per the above discussion. Assuming the SSC contributions to be similar in **Zn** and **Pd** the simulation parameters in Table 1 suggest that D_{SOC} in **Pd** is of the order of ca. -3 GHz.

As shown in Table 1, the spectral simulations of the trESR data predict that the **g**-tensor of the **Pd** system is aligned with the **D**-tensor with the following projections along the eigenframe of **D**: $g_x = 1.966$, $g_y = 2.011$, and $g_z = 2.006$. As can be seen from Eqs. (3) and (5), the anisotropy of the **g**-tensor is subject to the exact same group theoretical selection rules as the D_{SOC}-tensor. Hence, by symmetry, the largest negative g-shift is expected to be along the out-of-plane axis, as observed experimentally (g_x is the lowest).

The spin polarisation of **Pd** is given by the polarisation vector **P** $= (1.00, 0.00, 0.00)$ shown in Table 1. Since the D-value is negative, the D_x axis is the out-of-plane axis of **Pd** as shown in Fig. 4. Therefore, the spectral simulation predicts that spin polarisation is exclusively along the out of plane axis ($P_x = 1$). By symmetry, the direct SOC mechanism is only able to mediate ISC between the $^1B_{3u}$ state and the $^3B_{2u}$ state, or between $^1B_{2u}$ and $^3B_{3u}$. Whatever the ordering of the states, if internal conversion (IC) is assumed to be much faster than ISC, the resulting spin polarisation pattern is the same. The ISC process is allowed by the z-component of the SOC operator which transforms as B_{1g}. Therefore, the SOC matrix element, ξ, from Eq. (11) is expected to be exclusively in the molecular out-of-plane direction, i.e. the D_x axis, exactly as observed experimentally.

3.3. The dimer systems

Having elucidated the behaviour of the **Pd** system, the discussion of the dimer follows more easily. First of all, the Pd_2 system has a similar D-value to **Pd**, which is obvious by comparing the overall widths of the trESR spectra in Fig. 2. Furthermore, the ENDOR data in Fig. 6 confirm that the orientation of the **D**-tensor is the same in **Pd** and Pd_2. When the ENDOR spectra are recorded at the same field position in the trESR spectrum (either Z or XY), the peaks corresponding to the largest hyperfine coupling remain on the same side of the Larmor peak. Assuming that the largest hyperfine interaction in **Pd** (the beta proton marked in Figs. 4 and 6) maps to the same nucleus in Pd_2,
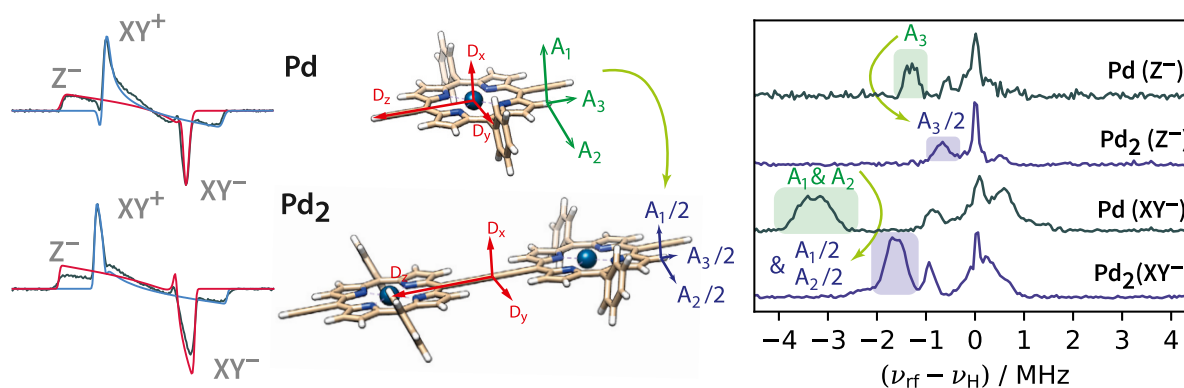
Fig. 6. Mims ^{1}H-ENDOR results on the **Pd** and **Pd$_2$** systems. The spectra were recorded at the field positions indicated in the diagrams on the left which represent the experimental trESR spectra and the simulated sub-spectra of the individual electron spin transitions (analogously to Fig. 4). The data are consistent with the same orientation of the **D**-tensor in both systems and with the fact that the spin density is delocalised in the dimer leading to a halving of the corresponding hyperfine couplings. The fact that the largest hyperfine peaks observed in measurements at almost the same field position remain on the same side of the Larmor peak proves that the orientation of the **D**-tensor is the same in both species.

then we may conclude that the pair of monomer/dimer ENDOR spectra correspond to a transition between the same pair of triplet sub-levels. Therefore, the sign and orientation of the **D**-tensor are the same. The same conclusion can be reached from MPS experiments performed on the **Pd$_2$** system, albeit the MPS effect is weaker in this system (see Figure S16).

As shown in Fig. 6, the magnitude of the largest hyperfine interaction is halved in **Pd$_2$** relative to **Pd**, indicating complete delocalisation of the spin density in the dimer. The same effect is observed in the ENDOR spectra of **Zn** vs. **Zn$_2$**, and **Fb** vs. **Fb$_2$** reported by Tait et al. [23]. The delocalisation of the spin density in the zinc and free-base dimers is responsible for the negative D-values of these systems (Table 1). The symmetry of the spin density changes from oblate to prolate, and since the SSC contribution is dominant in the **Zn$_2$** and **Fb$_2$** systems, the result is a change in the sign of D relative to the monomers. For **Pd$_2$**, the ENDOR data in Fig. 6 also suggest that the spin density becomes prolate (because the hyperfine coupling is halved), and so, the D_{SSC} value would change from positive to negative. This would be consistent with the previously mentioned similarity of the spin densities of the **Zn** and **Pd** systems (see Figure S19). However, the total D-value in **Pd$_2$** remains similar to the D-value of **Pd**. The conclusion is that the D_{SOC} contribution in **Pd$_2$** must decrease in magnitude by almost a factor of three (becoming of the order of -1 GHz). We have, unfortunately, been unable to establish why D_{SOC} decreases by a factor of three in the palladium dimer system, nor why this decrease is not mirrored by a significantly smaller **g**-anisotropy. Nonetheless, the crucial observation remains: had the SOC contribution been neglected from the discussion of the D-value in the palladium systems, the conclusions would have been dramatically erroneous. More precisely, if it were assumed that the D-values in **Pd** and **Pd$_2$** are only a dipolar effect, then it would follow that the two systems have the exact same spin density (which contradicts the ENDOR results).

Within error, the spin polarisation of the **Pd$_2$** system is approximately the same as **Pd**. There is, however, a small P_y contribution which could be caused by the vibronic mechanism. Although tentative, the assignment of this P_y value in **Pd$_2$** to the vibronic mechanism is motivated by the results of Tait et al. on the **Zn$_n$** series [23], which exhibited a progressive increase from $n = 1$ to 6 of one of the in-plane populations due to the vibronic mechanism. In the SI, it can be seen that the longer Pd^{2+} oligomers, **Pd$_n$**, have a greater tendency to remain out-of-plane polarised as the chain length increases cf. **Zn$_n$** [22]. This is most likely due to the larger direct SOC contribution to ISC in the presence of Pd^{2+}.

We now examine the ZFS, **g**-tensors and spin polarisation of the heterodimer systems, **PdFb** and **PdZn**. Inspection of the absolute values of D from Table 1 reveals that **PdFb** is effectively the same as **Fb**,

whereas **PdZn** is akin to **Zn$_2$**. This observation is validated by the data summarised in Fig. 7. In both systems, the palladium side appears to have a spin density deficit. As illustrated by the DFT computed spin densities (Fig. 7, top), the deficit on the palladium is less pronounced in the **PdZn** system relative to **PdFb**.

Precise quantification of the relative spin density on the two sides of the heterodimers is not a trivial problem. As an approximation, the average Mulliken spin populations may be explored. In the **PdFb** system, the absolute spin population is 83% localised on the free-base side. This is immediately clear from the diagram shown in the top left panel of Fig. 7. A Gaussian deconvolution (with 9 components) of the ENDOR spectra of **Fb** and **PdFb** reveals an average hyperfine coupling of -3.1 MHz for **PdFb**, and -3.4 MHz for **Fb**, with a corresponding ratio of 91%. These average values are calculated from the peaks below ca. -1 MHz because these correspond to the porphyrin protons (rather than side chain protons). Another noteworthy observation is that the peak between -6 and -4 MHz in **Fb** maps to two peaks in the same region of the **PdFb** spectrum. This may be consistent with the descent in symmetry of the heterodimer relative to **Fb**, leading to inequivalent hyperfine couplings. The assignment of these peaks is unclear; based on the DFT computed spin populations they may tentatively be assigned to two of the β-pyrrole protons on the free-base side of the molecule. For **PdZn**, an analysis of the spin populations is less conclusive than for **PdFb**. The average Mulliken spin population is predicted to be 58% localised on the *palladium* side, which is at odds with the spin density surface depicted in Fig. 7. This discrepancy in the average value is probably the result of the more severe non-uniformities of the spin density in this system (note how in the top right panel of Fig. 7, there are locally rather large contributions on the palladium side).

The free-base unit of **PdFb** contains most of the spin density which translates to a positive D-value in this system. The MPS data show this effect clearly: the X and Y peaks are enhanced when **E** ∥ **B**, i.e. τ is closely aligned with the D_x and D_y axes. Furthermore, by comparing the ENDOR spectra of **PdFb** and **Fb** recorded on the high-field side of the trESR spectra (the Z^- transition of **Fb**), we observe hyperfine features on the same side of the Larmor peak. This means that equivalent field positions in the trESR spectra correspond to the same electron spin transition, identified as $M_S = -1 \rightarrow 0$ for the **Fb** system, and so the sign of D is the same in both. The hyperfine couplings in **PdFb** are slightly smaller than the ones in **Fb**; this is because some of the spin density is on the palladium side. For the same reason, the larger value of λ in **PdFb** vs. **Fb** is reflective of the increased distortion from axiality of the spin density.

For **PdZn**, the MPS data are consistent with a negative D-value, just as expected for a system which is so similar to **Zn$_2$**. The X and Y features are diminished when **E** ∥ **B**, whereas the Z feature is enhanced.
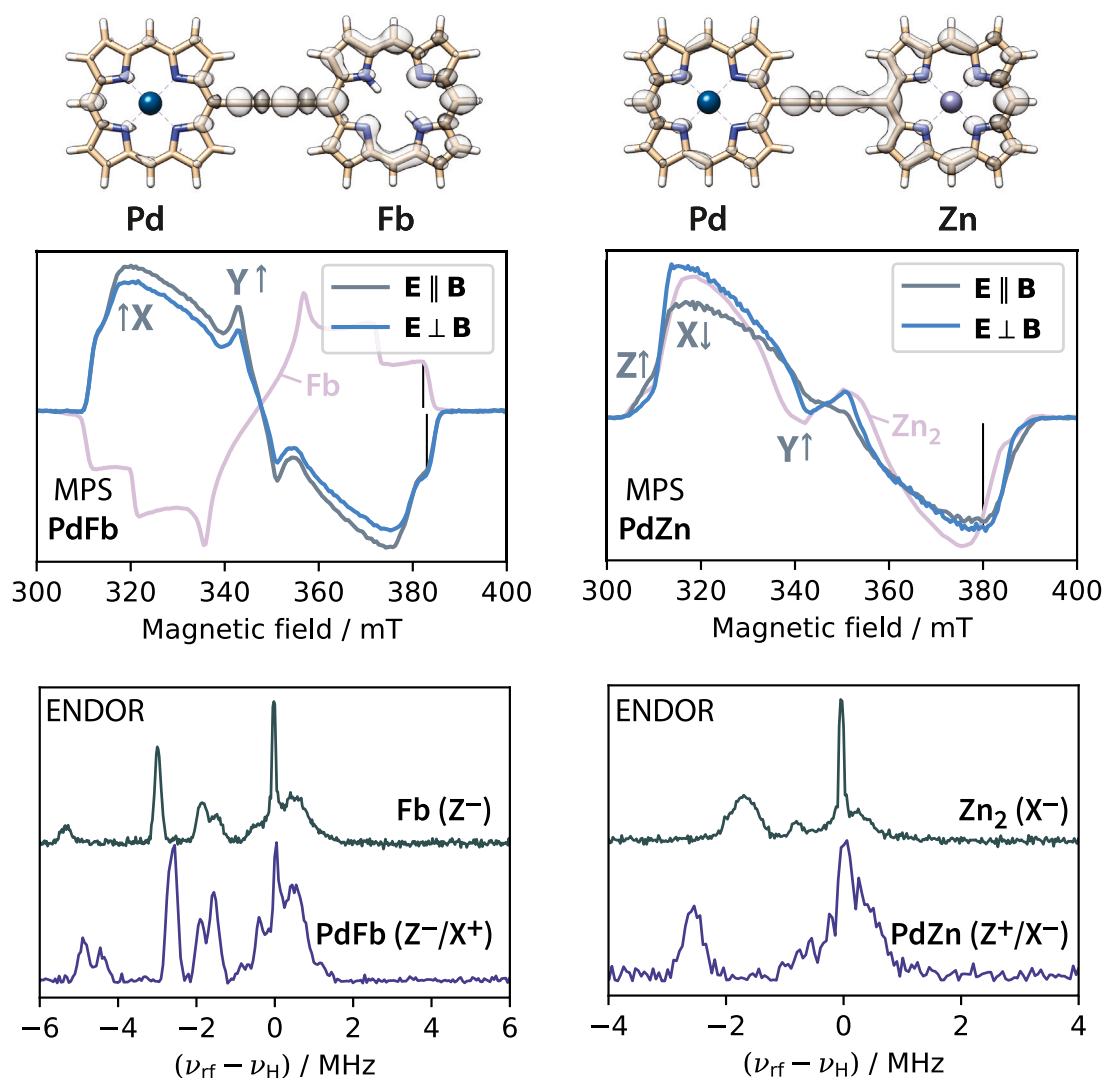
Fig. 7. (Top) DFT computed spin densities of the **PdFb** (left) and **PdZn** (right) triplet states. The calculations were performed in ORCA using the B3LYP functional in conjunction with the def2-SVP basis set for the light elements and def2-TZVPP for palladium and zinc [70]. These calculations are only for illustration purposes, hence the relatively small basis sets used. The spin density in the **PdFb** system is localised significantly on the free-base side. By contrast, in **PdZn**, the spin density is shifted slightly towards the zinc side. (Middle) Experimental MPS data obtained for the two heterodimer systems. The **PdFb** data were recorded at a wavelength of 550 nm whereas the **PdZn** data were recorded at 692 nm. Both of these excitation wavelengths correspond to the Q-band regions of the UV–Vis spectra (Figures S1–2). For **PdFb**, the labels indicate that there is an enhancement of the X and Y transitions when $\mathbf{E} \parallel \mathbf{B}$, in accordance with a positive D-value. For **PdZn**, the observed MPS effects are consistent with a negative D-value. In both panels, the usual (unpolarised) trESR spectra of the **Fb** and **Zn$_2$** are shown for comparison purposes. The black vertical lines indicate the field positions at which the ENDOR spectra were acquired. (Bottom) Mims ^{1}H-ENDOR spectra of the mixed dimers. The **PdFb** spectrum most closely resembles the spectrum of the **Fb** system, whereas **PdZn** is similar to **Zn$_2$**. The ENDOR data are in agreement with the interpretation of the MPS data and with the assignment of the sign of the D-values for the two heterodimers. In the mixed dimers, the larger orthorhombicity parameter causes the Z and X transitions to overlap more strongly (hence the labelling indicated in the bottom panels). For **PdFb** the ENDOR measurement corresponds to a dominant Z^- component (overlapping with a minor X^+ component), whereas for **PdZn** to a dominant X^- component (overlapping with a minor Z^+ component). This overlap of the different components is caused by the larger λ values of the heterodimer systems.

By the same arguments as outlined for **PdFb**, the ENDOR data also agree with the assignment of a negative D for **PdZn**. Importantly, the largest hyperfine coupling in **PdZn** is larger than the same coupling in **Zn$_2$**. This is because the spin density is partially localised on the zinc side of the heterodimer. It is also clear that the largest hyperfine coupling of the **PdZn** systems is intermediate in value between the **Zn** system (Fig. 4) and the **Zn$_2$** system (Fig. 7).

The spin polarisation reported in Table 1 for **PdZn** is the signature of a predominantly direct SOC mechanism for ISC. Both metals have sufficient SOC to account for this effect. By contrast, a remarkable spin polarisation effect is observed in the **PdFb** system: the ZFS parameters are the same as for **Fb** and yet, the trESR spectrum is inverted. The inversion is caused by the Pd^{2+} which drives the ISC process via the direct SOC mechanism, exactly as it did in all the other palladium porphyrin systems. Clearly, the photophysical cascade of events initiated

by light excitation of **PdFb** must involve an intermediate excited state which has a significant coefficient on the palladium ion. Unfortunately, attempts to capture such an intermediate excited state via trESR have been unsuccessful: the trESR signature of **PdFb** shows only a uniform decrease in signal intensity as a function of time after laser excitation (*i.e.* no change in ZFS or spin polarisation), and measurements at different wavelengths yielded identical spectra (see Figures S17 and S18). It is very likely that this intermediate is part of the prompt dynamics occurring on a sub-nanosecond time scale (undetectable by trESR). However, the importance of the **PdFb** systems lies in the fact that by photoexcitation, almost the exact same spin density is formed as for the **Fb** system, yet the spin polarisation of the former is almost exclusively out-of-plane rather than the typical in-plane spin polarisation of the latter. In an alternative perspective, the inclusion of one Pd^{2+} ion

into the **Fb₂** structure pushes the spin density to the other side of the molecule and causes an out-of-plane spin polarisation.

4. Conclusions

The work presented here describes the influence of the SOC interaction on the spin Hamiltonian parameters and spin polarisation of porphyrin monomers and dimers. This issue was addressed by analysing the trends in D and **P** in a series of porphyrin systems with/without palladium including previously published results relating to zinc and free-base porphyrin oligomers [22,23,26,29]. An understanding of the relationship between the symmetry of the spin density and the ISC mechanisms in **Zn**, **Zn₂**, **Fb**, and **Fb₂** guided the interpretation of the data for all Pd^{2+} porphyrins. The results of trESR, MPS, and ^{1}H-ENDOR showed that the D-value in the palladium systems is dominated by the SOC contribution and that the sign of D is negative throughout the series. The SOC contribution complicates the interpretation of the ZFS of the palladium porphyrins, a problem which was addressed here from the vantage point of group theory. Nonetheless, it was found that the dipolar contribution to D is largely unaffected by the presence of Pd^{2+}; except for the heterodimer systems, **PdFb** and **PdZn**, which featured partially localised spin densities. The main difference is that all palladium systems have a predominantly out-of-plane spin polarisation due to the direct SOC mechanism mediated by the heavy metal. Regarding spintronics, we envisage integrating Pd^{2+} into future oligoporphyrin molecular wires as a way of controlling spin polarisation without compromising the delocalisation length of the spin density.

Declaration of competing interest

The authors declare that they have no known competing financial interests or personal relationships that could have appeared to influence the work reported in this paper.

Data availability

Data will be made available on request.

Acknowledgements

Appendix A. Supplementary data

Supplementary material related to this article can be found online at https://doi.org/10.1016/j.jmr.2023.107546.

References

[1] S.A. Wolf, D.D. Awschalom, R.A. Buhrman, J.M. Daughton, v.S. von Molnár, M.L. Roukes, A.Y. Chtchelkanova, D.M. Treger, Spintronics: A spin-based electronics vision for the future, Science 294 (5546) (2001) 1488–1495, http://dx.doi.org/10.1126/science.1065389.

[2] S.A. Wolf, A.Y. Chtchelkanova, D.M. Treger, Spintronics—A retrospective and perspective, IBM J. Res. Dev. 50 (1) (2006) 101–110, http://dx.doi.org/10.1147/rd.501.0101.

[3] P.J. Rajput, S.U. Bhandari, G. Wadhwa, A review on—Spintronics an emerging technology, Silicon (2022) 1–16, http://dx.doi.org/10.1007/s12633-021-01643-x.

[4] O. Ostroverkhova, Handbook of Organic Materials for Optical and (Opto) Electronic Devices: Properties and Applications, Elsevier, 2013, http://dx.doi.org/10.1533/9780857098764.

[5] I. Žutić, J. Fabian, S.D. Sarma, Spintronics: Fundamentals and applications, Rev. Modern Phys. 76 (2) (2004) 323, http://dx.doi.org/10.1103/RevModPhys.76.323.

[6] I. Bergenti, V. Dediu, M. Prezioso, A. Riminucci, Organic spintronics, Phil. Trans. R. Soc. A 369 (1948) (2011) 3054–3068, http://dx.doi.org/10.1098/rsta.2011.0155.

[7] Z.H. Xiong, D. Wu, Z. Valy Vardeny, J. Shi, Giant magnetoresistance in organic spin-valves, Nature 427 (6977) (2004) 821–824, http://dx.doi.org/10.1038/nature02325.

[8] H. Uoyama, K. Goushi, K. Shizu, H. Nomura, C. Adachi, Highly efficient organic light-emitting diodes from delayed fluorescence, Nature 492 (7428) (2012) 234–238, http://dx.doi.org/10.1038/nature11687.

[9] F.B. Dias, K.N. Bourdakos, V. Jankus, K.C. Moss, K.T. Kamtekar, V. Bhalla, J. Santos, M.R. Bryce, A.P. Monkman, Triplet harvesting with 100% efficiency by way of thermally activated delayed fluorescence in charge transfer OLED emitters, Adv. Mater. 25 (27) (2013) 3707–3714, http://dx.doi.org/10.1002/adma.201300753.

[10] K.S. Kiran, V. Preethi, S. Kumar, A brief review of organic solar cells and materials involved in its fabrication, Mater. Today-Proc. (2022) http://dx.doi.org/10.1016/j.matpr.2022.02.205.

[11] C.M. Marian, Understanding and controlling intersystem crossing in molecules, Annu. Rev. Phys. Chem. 72 (2021) 617–640, http://dx.doi.org/10.1146/annurev-physchem-061020-053433.

[12] H.L. Anderson, Building molecular wires from the colours of life: conjugated porphyrin oligomers, Chem. commun. (23) (1999) 2323–2330, http://dx.doi.org/10.1039/A904209A.

[13] G. Sedghi, V.M. García-Suárez, L.J. Esdaile, H.L. Anderson, C.J. Lambert, S. Martín, D. Bethell, S.J. Higgins, M. Elliott, N. Bennett, M.J. E., Long-range electron tunnelling in oligo-porphyrin molecular wires, Nat. Nanotechnol. 6 (8) (2011) 517–523, http://dx.doi.org/10.1038/nnano.2011.111.

[14] G. Sedghi, K. Sawada, L.J. Esdaile, M. Hoffmann, H.L. Anderson, D. Bethell, W. Haiss, S.J. Higgins, R.J. Nichols, Single molecule conductance of porphyrin wires with ultralow attenuation, J. Am. Chem. Soc. 130 (27) (2008) 8582–8583, http://dx.doi.org/10.1021/ja802281c.

[15] B.K. Kang, N. Aratani, J.K. Lim, D. Kim, A. Osuka, K.-H. Yoo, Length and temperature dependence of electrical conduction through dithiolated porphyrin arrays, Chem. Phys. Lett. 412 (4–6) (2005) 303–306, http://dx.doi.org/10.1016/j.cplett.2005.07.008.

[16] D.H. Yoon, S.B. Lee, K.-H. Yoo, J. Kim, J.K. Lim, N. Aratani, A. Tsuda, A. Osuka, D. Kim, Electrical conduction through linear porphyrin arrays, J. Am. Chem. Soc. 125 (36) (2003) 11062–11064, http://dx.doi.org/10.1021/ja0346429.

[17] P.J. Angiolillo, V.S.-Y. Lin, J.M. Vanderkooi, M.J. Therien, EPR spectroscopy and photophysics of the lowest photoactivated triplet state of a series of highly conjugated (porphinato)Zn arrays, J. Am. Chem. Soc. 117 (50) (1995) 12514–12527, http://dx.doi.org/10.1021/ja00155a015.

[18] R. Shediac, M.H.B. Gray, H.T. Uyeda, R.C. Johnson, J.T. Hupp, P.J. Angiolillo, M.J. Therien, Singlet and triplet excited states of emissive, conjugated bis(porphyrin) compounds probed by optical and EPR spectroscopic methods, J. Am. Chem. Soc. 122 (29) (2000) 7017–7033, http://dx.doi.org/10.1021/ja9939587.

[19] P.J. Angiolillo, K. Susumu, H.T. Uyeda, L.V. S.-Y, R. Shediac, M.J. Therien, Trends in triplet excitation delocalization in highly conjugated (porphinato)zinc(II) arrays probed by EPR spectroscopy, Synthetic Met. 116 (1) (2001) 247–253, http://dx.doi.org/10.1016/S0379-6779(00)00461-6.

[20] P.J. Angiolillo, H.T. Uyeda, T.V. Duncan, M.J. Therien, Impact of electronic asymmetry on photoexcited triplet-state spin distributions in conjugated porphyrin oligomers probed via EPR spectroscopy, J. Phys. Chem. B 108 (32) (2004) 11893–11903, http://dx.doi.org/10.1021/jp040032z.

[21] P.J. Angiolillo, J. Rawson, P.R. Frail, M.J. Therien, The evolution of spin distribution in the photoexcited triplet state of ethyne-elaborated porphyrins, Chem. Commun. 49 (2013) 9722–9724, http://dx.doi.org/10.1039/C3CC44903C.

[22] C.E. Tait, P. Neuhaus, H.L. Anderson, C.R. Timmel, Triplet state delocalization in a conjugated porphyrin dimer probed by transient electron paramagnetic resonance techniques, J. Am. Chem. Soc. 137 (20) (2015) 6670–6679, http://dx.doi.org/10.1021/jacs.5b03249.

[23] C.E. Tait, P. Neuhaus, M.D. Peeks, H.L. Anderson, C.R. Timmel, Transient EPR reveals triplet state delocalization in a series of cyclic and linear π-conjugated porphyrin oligomers, J. Am. Chem. Soc. 137 (25) (2015) 8284–8293, http://dx.doi.org/10.1021/jacs.5b04511.

[24] M.D. Peeks, C.E. Tait, P. Neuhaus, G.M. Fischer, M. Hoffmann, R. Haver, A. Cnossen, J.R. Harmer, C.R. Timmel, H.L. Anderson, Electronic delocalization in the radical cations of porphyrin oligomer molecular wires, J. Am. Chem. Soc. 139 (30) (2017) 10461–10471, http://dx.doi.org/10.1021/jacs.7b05386.

[25] C.E. Tait, P. Neuhaus, H.L. Anderson, C.R. Timmel, D. Carbonera, M. Di Valentin, HYSCORE on photoexcited triplet states, Appl. Magn. Reson. 46 (4) (2015) 389–409, http://dx.doi.org/10.1007/s00723-014-0624-5.

[26] S. Richert, C.E. Tait, C.R. Timmel, Delocalisation of photoexcited triplet states probed by transient EPR and hyperfine spectroscopy, J. Magn. Reson. 280 (2017) 103–116, http://dx.doi.org/10.1016/j.jmr.2017.01.005.

[27] S. Richert, B. Limburg, H.L. Anderson, C.R. Timmel, On the influence of the bridge on triplet state delocalization in linear porphyrin oligomers, J. Am. Chem. Soc. 139 (34) (2017) 12003–12008, http://dx.doi.org/10.1021/jacs.7b06518.

[28] S. Richert, G. Bullard, J. Rawson, P.J. Angiolillo, M.J. Therien, C.R. Timmel, On the importance of electronic symmetry for triplet state delocalization, J. Am. Chem. Soc. 139 (15) (2017) 5301–5304, http://dx.doi.org/10.1021/jacs.7b01204.

[29] A.J. Redman, G. Moise, S. Richert, E.J. Viere, W.K. Myers, M.J. Therien, C.R. Timmel, EPR of photoexcited triplet-state acceptor porphyrins, J. Phys. Chem. C 125 (21) (2021) 11782–11790, http://dx.doi.org/10.1021/acs.jpcc.1c03278.

[30] G. Moise, L. Tejerina, M. Rickhaus, H.L. Anderson, C.R. Timmel, Spin delocalization in the radical cations of porphyrin molecular wires: A new perspective on EPR approaches, J. Phys. Chem. Lett. 10 (19) (2019) 5708–5712, http://dx.doi.org/10.1021/acs.jpclett.9b02262.

[31] M. Asano-Someda, A. van der Est, U. Krüger, D. Stehlik, Y. Kaizu, H. Levanon, Intramolecular energy transfer in a covalently linked copper (II) porphyrin- free base porphyrin dimer: novel spin polarization in the energy acceptor, J. Phys. Chem. A 103 (34) (1999) 6704–6714, http://dx.doi.org/10.1021/jp9912096.

[32] M. Bennati, K. Németh, P.R. Surján, M. Mehring, Zero-field-splitting and π-electron spin densities in the lowest excited triplet state of oligothiophenes, J. Chem. Phys. 105 (11) (1996) 4441–4447, http://dx.doi.org/10.1063/1.472296.

[33] F. Lendzian, R. Bittl, W. Lubitz, Pulsed ENDOR of the photoexcited triplet states of bacteriochlorophyll a and of the primary donor P865 in reaction centers of rhodobacter sphaeroides R-26, Photosynth. Res. 55 (2) (1998) 189–197, http://dx.doi.org/10.1023/A:1006030221445.

[34] M. Huber, A.A. Doubinskii, C.W.M. Kay, K. Möbius, ENDOR on the triplet state of the primary electron donor in the photosynthetic bacterium rhodobacter sphaeroides—One step forward in a still unfinished story, Appl. Magn. Reson. 13 (3) (1997) 473–485, http://dx.doi.org/10.1007/BF03162221.

[35] R.H. Clarke, D.R. Hobart, W.R. Leenstra, The triplet state of the chlorophyll dimer, J. Am. Chem. Soc. 101 (9) (1979) 2416–2423, http://dx.doi.org/10.1021/ja00503a030.

[36] H. Levanon, J.R. Norris, The photoexcited triplet state and photosynthesis, Chem. Rev. 78 (3) (1978) 185–198, http://dx.doi.org/10.1021/cr60313a001.

[37] M.C. Thurnauer, J.R. Norris, The ordering of the zero field triplet spin sublevels in the chlorophylls. a magnetophotoselection study, Chem. Phys. Lett. 47 (1) (1977) 100–105, http://dx.doi.org/10.1016/0009-2614(77)85315-3.

[38] P.K. Poddutoori, Y.E. Kandrashkin, C.O. Obondi, F. D'Souza, A. van der Est, Triplet electron transfer and spin polarization in a palladium porphyrin–fullerene conjugate, Phys. Chem. Chem. Phys. 20 (44) (2018) 28223–28231, http://dx.doi.org/10.1039/C8CP04937H.

[39] H. Miwa, K. Ishii, N. Kobayashi, Electronic structures of zinc and palladium tetraazaporphyrin derivatives controlled by fused benzo rings, Chem.– Eur. J. 10 (18) (2004) 4422–4435, http://dx.doi.org/10.1002/chem.200400328.

[40] Y. Mulyana, K. Ishii, A novel aspect of spectroscopy for porphyrinic compounds under magnetic fields, Dalton T. 43 (47) (2014) 17596–17605, http://dx.doi.org/10.1039/C4DT01428F.

[41] C.O. Obondi, B. Lim, P.K. Poddutoori, A. van der Est, F. D'Souza, Modulating the generation of long-lived charge separated states exclusively from the triplet excited states in palladium porphyrin–fullerene conjugates, Nanoscale 8 (15) (2016) 8333–8344, http://dx.doi.org/10.1039/C6NR01083K.

[42] Y. Gao, V. Piradi, X. Zhu, S.K. So, Palladium (II) and platinum (II) porphyrin donors for organic photovoltaics, ACS Appl. Ener. Mater. 5 (4) (2022) 4916–4925, http://dx.doi.org/10.1021/acsaem.2c00317.

[43] W. Crisp, S.A. Fagan-Avery, B.M. Campbell, D.R. Morphet, K.G. Reynolds, B. Kudisch, M.I. Gonzalez, S.-L. Zheng, D.K. Dogutan, D.G. Nocera, Comparative excited state dynamics of metallo meso-(4-fluoro-2, 6-dimethyl-phenyl) porphyrins, Inorg. Chem. Commun. 146 (2022) 109999, http://dx.doi.org/10.1016/j.inoche.2022.109999.

[44] Y. Bai, J.-H. Olivier, H. Yoo, N.F. Polizzi, J. Park, J. Rawson, M.J. Therien, Molecular road map to tuning ground state absorption and excited state dynamics of long-wavelength absorbers, J. Am. Chem. Soc. 139 (46) (2017) 16946–16958, http://dx.doi.org/10.1021/jacs.7b09982.

[45] T.V. Duncan, P.R. Frail, I.R. Miloradovic, M.J. Therien, Excitation of highly conjugated (porphinato) palladium (II) and (porphinato) platinum (II) oligomers produces long-lived, triplet states at unit quantum yield that absorb strongly over broad spectral domains of the NIR, J. Phys. Chem. B 114 (45) (2010) 14696–14702, http://dx.doi.org/10.1021/jp102901u.

[46] G. Hanson, L. Berliner, High Resolution EPR: Applications to Metalloenzymes and Metals in Medicine, Vol. 28, Springer Science & Business Media, 2009, http://dx.doi.org/10.1007/978-0-387-84856-3.

[47] R. McWeeny, On the origin of spin-Hamiltonian parameters, J. Chem. Phys. 42 (5) (1965) 1717–1725, http://dx.doi.org/10.1063/1.1696183.

[48] M. Kaupp, M. Buhl, V.G. Malkin, Calculation of NMR and EPR Parameters, Wiley Online Library, 2004, http://dx.doi.org/10.1002/3527601678.

[49] F. Neese, Sum-over-states based multireference ab initio calculation of EPR spin Hamiltonian parameters for transition metal complexes. A case study, Magn. Reson. Chem. 42 (S1) (2004) S187–S198, http://dx.doi.org/10.1002/mrc.1456.

[50] K. Sugisaki, K. Toyota, K. Sato, D. Shiomi, M. Kitagawa, T. Takui, Quantum chemical calculations of the zero-field splitting tensors for organic spin multiplets, EPR Free Radicals Solids I: Trends Methods Appl. (2013) 363–392, http://dx.doi.org/10.1007/978-94-007-4893-48.

[51] G. Moise, Exploiting EPR to Elucidate Fine and Hyperfine Interactions in Complex Chemical and Biological Systems, University of Oxford, 2020.

[52] A. Carrington, A.D. McLachlan, Introduction to Magnetic Resonance, with Applications to Chemistry and Chemical Physics, Chapman and Hall, 1967.

[53] S.P. McGlynn, T. Azumi, Molecular Spectroscopy of the Triplet State, Prentice-Hall, 1969.

[54] P.W. Atkins, R.S. Friedman, Molecular Quantum Mechanics, Oxford University Press, 2011.

[55] C.M. Marian, Spin–orbit coupling and intersystem crossing in molecules, Wires. Comput. Mol. Sci. 2 (2) (2012) 187–203, http://dx.doi.org/10.1002/wcms.83.

[56] F. Neese, E.I. Solomon, Calculation of zero-field splittings, g-values, and the relativistic nephelauxetic effect in transition metal complexes. Application to high-spin ferric complexes, Inorg. chem. 37 (26) (1998) 6568–6582, http://dx.doi.org/10.1021/ic980948i.

[57] M.A. El-Sayed, Spin—orbit coupling and the radiationless processes in nitrogen heterocyclics, J. Chem. Phys. 38 (12) (1963) 2834–2838, http://dx.doi.org/10.1063/1.1733610.

[58] W.G. van Dorp, W.H. Schoemaker, M. Soma, J.H. van der Waals, The lowest triplet state of free base porphin. Determination of its kinetics of populating and depopulating from microwave-induced transients in the fluorescence intensity, Mol. Phys. 30 (6) (1975) 1701–1721, http://dx.doi.org/10.1080/00268977500103231.

[59] S. Stoll, A. Schweiger, EasySpin, A comprehensive software package for spectral simulation and analysis in EPR, J. Magn. Reson. 178 (1) (2006) 42–55, http://dx.doi.org/10.1016/j.jmr.2005.08.013.

[60] C.E. Tait, M.D. Krzyaniak, S. Stoll, Computational tools for the simulation and analysis of spin-polarized EPR spectra, J. Magn. Reson. 349 (2023) 107410, http://dx.doi.org/10.1016/j.jmr.2023.107410.

[61] S. Perun, J. Tatchen, C.M. Marian, Singlet and triplet excited states and intersystem crossing in free-base porphyrin: TDDFT and DFT/MRCI study, ChemPhysChem 9 (2) (2008) 282–292, http://dx.doi.org/10.1002/cphc.200700509.

[62] I.Y. Chan, W.G. van Dorp, T. Schaafsma, J. van der Waals, The lowest triplet state of Zn porphin, Mol. Phys. 22 (5) (1971) 741–751, http://dx.doi.org/10.1080/00268977100103061.

[63] I. Chan, W. van Dorp, T. Schaafsma, J. van der Waals, The lowest triplet state of Zn porphin, Mol. Phys. 22 (5) (1971) 753–760, http://dx.doi.org/10.1080/00268977100103071.

[64] R.L. Ake, M. Gouterman, Porphyrins XIV. Theory for the luminescent state in VO, Co, Cu complexes, Theor. Chim. Acta 15 (1969) 20–42, http://dx.doi.org/10.1007/BF00526463.

[65] H.S. Judeikis, S. Siegel, Magnetophotoselection. Effect of depopulation and triplet-triplet absorption, J. Phys. Chem. 74 (6) (1970) 1228–1235, http://dx.doi.org/10.1021/j100701a012.

[66] M.C. Thurnauer, J.R. Norris, Magnetophotoselection applied to the triplet state observed by EPR in photosynthetic bacteria, Biochem. Bioph. Res. Co. 73 (2) (1976) 501–506, http://dx.doi.org/10.1016/0006-291X(76)90735-X.

[67] M.C. Thurnauer, J.R. Norris, The ordering of the zero field triplet spin sublevels in the chlorophylls. A magnetoselection study, Chem. Phys. Lett. 47 (1) (1977) 100–105, http://dx.doi.org/10.1016/0009-2614(77)85315-3.

[68] A. Antipas, M. Gouterman, Porphyrins. 44. Electronic states of cobalt, nickel, rhodium, and palladium complexes, J. Am. Chem. Soc. 105 (15) (1983) 4896–4901, http://dx.doi.org/10.1021/ja00353a009.

[69] M. Gouterman, G.H. Wagnière, L.C. Snyder, Spectra of porphyrins: Part II. Four orbital model, J. Mol. Spectrosc. 11 (1–6) (1963) 108–127, http://dx.doi.org/10.1016/0022-2852(63)90011-0.

[70] F. Neese, The ORCA program system, Wires. Comput. Mol. Sci. 2 (1) (2012) 73–78, http://dx.doi.org/10.1002/wcms.81.